Check for updates

Cesium lead bromide as a colorimetric and fluorometric sensing platform for the selective detection of uric acid†

Priyankamoni Saikia, Jayashree Nath, Swapan Kumar Dolui ⓘ* and Sanjeev Pran Mahanta ⓘ*

Chapter 2

"Cesium Lead Bromide as a colorimetric and fluorometric sensing platform for selective detection of Uric Acid"

Highlights: The selected perovskite material explores as sensing material for detection of uric acid. Based on both fluorescence and colorimetric technique, the chapter discusses detailed studies on detection limit, stability towards real samples and mechanism of sensing process.

Saikia, P., Nath, J., Dolui, S. K., and Mahanta, S. P. Cesium Lead Bromide as a colorimetric and fluorometric sensing platform for selective detection of Uric Acid. *New Journal of Chemistry*, 2023 (just accepted, DOI: 10.1039/D3NJ00202K).
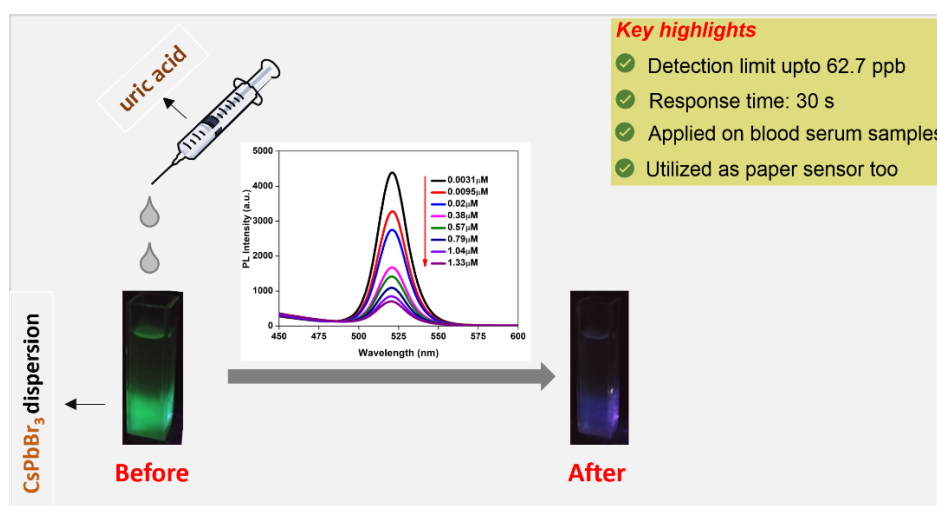
2.1 Introduction

Uric Acid (UA) is an oxidized product of purine metabolism, and it is an important biological indicator for metabolic status and diseases related to purine (Figure 2.1) [1-3]. Normally, the physiological range of uric acid is 0.13-0.46 mM (26-60 ppm) in blood serum [4]. When the concentration of UA exceeds this optimal level, it is known as hyperuricemia, and several diseases such as gout, arthritis, chronic nephropathy, etc. can be possible in that state [5-7]. On the other hand, hypouricemia (the lower level of UA) causes diseases such as multiple sclerosis or Parkinson's disease [8,9]. To maintain a healthy UA level in our blood serum, an accurate assessment of UA levels in urine or blood serum is of paramount importance to avoid UA-related diseases.
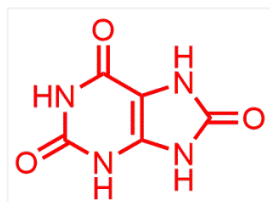

Figure 2.1 Molecular structure of uric acid

To detect UA at an accurate level, some common detection technologies including Raman spectroscopy, chromatography, capillary electrophoreses, etc. [10-15] are mostly used. However, most of these methods requires expensive techniques, highly time-consuming operations and thereby, these are not suitable for rapid detection processes. The strategy based on enzyme sensing and electrochemical sensing are another known methods for uric acid detection. These two sensors have problem in selectivity test, similar analytes such as ascorbic acid (AA) during the electrochemical detection method of uric acid. The identical oxidation peak potential of ascorbic acid and uric acid causes some difficulties to distinguish the UA from AA in electrochemical detection method. Also, during the enzyme sensing process, deposition takes a longer time thus making them unsuitable for the detection of UA [16]. In that context, sensing method showcasing facile, rapid, selective, and sensitive analytical method for the determination of the accurate concentration of UA in practical value is highly beneficial. The fluorescence chemo-sensors have attracted considerable attention due to their high sensitivity, rapid response, high selectivity, simple operation, low cost, and lower detection limits towards the guest analytes

[17-23]. During detection processes, the commonly adopted fluorescence mechanisms are Forster resonance electron transfer, and intramolecular charge transfer. Furthermore, various materials are used as fluorescence probes, such as metal-organic frameworks (MOF) [24,25], polymers [25], quantum dots [26], carbon dots [27], etc.

All inorganic halide perovskites have attracted much attention in recent years due to their diverse applications [28]. Among them, the cesium lead bromide (CsPbBr$_3$) perovskites are most studied inorganic halide perovskites due to their relatively higher air-stable property compared to other inorganic-organic halide perovskites. They are associated with the advantage of higher photoluminescence quantum yield, narrow emission peak, high photoelectric conversion efficiency, long carrier lifetimes, and long diffusion coefficients [29]. Owing to their outstanding optoelectronic advantageous properties, they have wide applications in various fields such as light-emitting diodes [30], optoelectronic devices [31], photodetectors [32], and solar cells [33] (Figure 2.2).
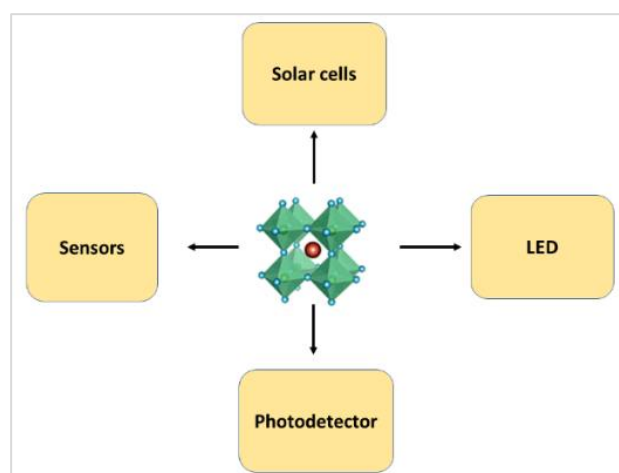

Figure 2.2 Applications of CsPbBr$_3$ in various fields

In addition, they are employed as a suitable candidate to develop as photoluminescent (PL) sensor probes due to the tunable optical and electronic properties of halide perovskites. Apart from being photoluminescence, they also act as chemiluminescent, electroluminescent, and colorimetric sensor probes for detecting humidity, gas molecules, metal ions, pesticides, etc. Among them, the PL sensing mode is one of the most frequently used methods for the detection of target analytes. The material can trigger some significant structural and compositional

changes in the precursor solutions and thereby, it shows to either turn on or off the response of the respective PL signal. Owing to the instability towards humid conditions and polar solvents, few works have been reported where halide perovskites are employed as a chemo/biosensor. Chen and co-workers reported $MAPbBr_3$ nanoparticles in the SiO_2 nanosphere as a PL turn-on method for its application towards methylamine gas where interaction between methylamine and $HPbBr_3/PbBr_2@SiO_2$ was mentioned [36]. Deriving a similar concept about the bright luminescence featuring a higher quantum yield of $CsPbBr_3$ perovskites, we hypothesized that $CsPbBr_3$ perovskites could also be used as a fluorescence probe to detect analytes. Ma and co-workers demonstrated $CsPbBr_3$ as an HCl vapor sensor probe [37]. Similarly, Feng and co-workers recently reported $CsPbBr_3$ as a fluorescence sensor probe to detect total polar molecules in edible oils [38].

In this chapter, the work was focused on the bright green luminescent $CsPbBr_3$ perovskites as a fluorescence and colorimetric sensing probe for detecting Uric acid (UA). Furthermore, the designed sensor probe was successfully applied to detect uric acid levels in real sample assay in human blood serum.

2.2 Experimental

2.2.1 Materials

All chemicals were purchased from suppliers and used without purification. Cesium Bromide (CsBr) (99.9%, Alfa Aesar), Lead Bromide ($PbBr_2$) (99.9%, TCI), Dimethyl Sulfoxide (DMSO) (99%, Alfa Aesar), Toluene (99%, Alfa Aesar), Uric Acid (Sigma Aldrich), Urea (Sisco Research Laboratories), Glycine (Alfa Aesar), Ascorbic Acid (Alfa Aesar), Uracil (Alfa Aesar), Alanine (Sigma Aldrich), Glucose (Sigma Aldrich), Adenine (Alfa Aesar), Cystine (Alfa Aldrich), NaCl (SRL), KCl (SRL), Creatinine (Sigma Aldrich), Hippuric Acid (TCI) were commercially available.

2.2.2 Synthesis of inorganic halide perovskite ($CsPbBr_3$)

The $CsPbBr_3$ perovskites was synthesized by using the traditional one-pot anti-solvent method at room temperature [39]. 2.5 mmol (0.5320 g) of CsBr and 2 mmol (0.734 g) of $PbBr_2$ were mixed into 15 mL DMSO. The solution was then stirred for 12 h to form a clear precursor solution. Later, the solution was quickly injected into 150 mL of toluene under vigorous stirring. The passivated $CsPbBr_3$ crystals were

centrifuged and washed with toluene and placed in a vacuum oven at 80 ℃ to obtain the dried and pure compound.

2.2.3 Structural Characterization

The fluorescence emission spectra were recorded using a Hitachi F-2700 fluorescence spectrophotometer at room temperature. The decay of fluorescence spectra was measured by using (Horiba Scientific, instrument) model. The surface morphologies of CsPbBr$_3$ metal halide perovskites (MHPs) were analysed by using Gemini 500 FE-SEM instrument and energy dispersive compositional mappings were recorded by using SEM (JEOL-JSM-6390LV). The High-resolution Transmission Electron Microscope (HR-TEM) images were captured using (JEM-2100, JEOL, USA). XRD was measured with Bruker D8 advanced eco P-XRD system. FT-IR spectra of the samples were performed using a Nicolet Impact-410 IR spectrometer (USA) in the KBr medium at room temperature in the range of 4000–400 cm^{-1}. A Shimadzu UV-2550 spectrophotometer was used to record the electronic absorption spectra of the samples in the wavelength range of 200-800 nm. The chemical compositions were analysed by X-ray photoelectron spectroscopy (Perkin Elmer model 1257), instrument.

2.2.4 Fluorescence measurements

The relative photoluminescence quantum yield of the synthesized perovskite crystals was measured using Rhodamine B as a reference (Quantum Yield = 97% in ethanol) applying the following equation [40,41].

$$\Phi_{fx} = \frac{\eta_x^2}{\eta_{Rhodamine\ Blue}^2} \cdot \frac{A_{Rhodamine\ Blue}}{A_x} \cdot \frac{F_x}{F_{Rhodamine\ Blue}} \cdot \Phi_{fRhodamine\ Blue}$$

In this equation, η is the refractivity (η = 1.36 for ethanol and η = 1.49 for toluene), A is the absorbance which is lower than 0.01 to avoid internal filter effects [41] and F is the integral absorption area in the luminescence spectra.

2.2.5 Stability study

To measure the stability of synthesized perovskites, initially 0.1 mmol of CsPbBr$_3$ (0.057 g) was dispersed in 10 mL toluene and sonicated for 30 min to get a homogeneous mixture. Then, 3 mL of perovskite solution was taken in a cuvette and their respective luminescence peak was recorded under the excitation wavelength of

380 nm at different interval of time under 80% humid condition. Similarly, the subsequent photostability test was performed with dispersion 0.1 mmol of perovskite in a 10 mL toluene. Again, 3 mL from the above solution was taken as a stock solution. The solution was further illuminated under the wavelength of 365 nm UV-lamp for a period of 8 hours. Their changes in PL intensity were measured under the excitation wavelength of 380 nm.

2.2.6 Fluorescence Assay of Uric-Acid using CsPbBr$_3$-based sensor

To carry out the selectivity and sensitivity of CsPbBr$_3$ dispersion towards UA detection, a suspension of CsPbBr$_3$ perovskite in toluene having a concentration of (0.57 g/100 mL) was prepared and sonicated for 30 mins to get a homogeneous suspension. Then, 3 mL of this suspension was placed in a quartz cuvette and to that 50 µL volume of UA solution with known concentration was added. The fluorescence intensity of the suspension was measured by exciting the solution with a wavelength of 380 nm.

2.2.7 The paper-based sensor of the perovskite CsPbBr$_3$ for UA sensing

To validate the visual detection of Uric Acid by CsPbBr$_3$, a paper sensor was fabricated where 1 mL of dispersed perovskite solutions were first added to 1cm×1cm cellulose paper. After a few minutes, various concentrations of UA were dripped into the following paper. The fluorescence colour response was observed under the UV emitting lamp of 365 nm wavelength.

2.2.8 Detection of Uric Acid in real samples

To investigate the practical applicability of the designed sensor, further the sensing abilities in human blood serum samples were studied. The blood serum samples were collected from Health Centre, Tezpur University with the complete agreement and obeying their assigned rules and regulations. Then, the samples were diluted 100 times and mixed with different concentrations of UA for fluorescence measurements. The respective fluorescence spectra of the samples were measured with excitation wavelength of 380 nm. Further, the recovery rate of the blood samples was calculated.

2.3 Results and Discussion

2.3.1 Structural Analysis

2.3.1.1 XRD analysis

Generally, $CsPbBr_3$ perovskite exhibits cubic, orthorhombic, and tetragonal phases [42]. The X-ray diffraction (XRD) pattern of $CsPbBr_3$ was recorded to analyze the crystal structure of the synthesized perovskites (Figure 2.3). The diffraction peaks (110), (112), and (220) indexed at 15.19, 21.48, and 30.58 agrees well with the standard orthorhombic phase of perovskite crystal [43].
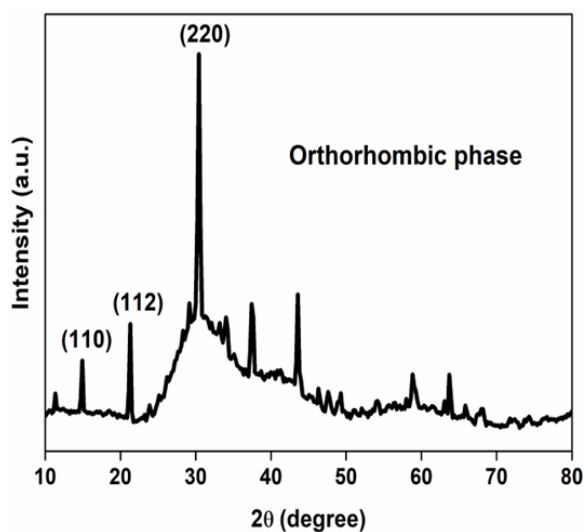

Figure 2.3 XRD spectra of $CsPbBr_3$ crystal

2.3.1.2 Energy Dispersive X-ray (EDX) analysis

The elemental information of $CsPbBr_3$ was analysed by EDX analysis. As depicted in Figure 2.4a, (EDX) analysis reveals the existence of elements Cs, Pb, and Br with their atomic percentage 1.4:1:3.6 with a close approximation to their stoichiometric ratios. The elemental image of perovskite also depicts the homogeneous distribution of all the elements in the synthesized crystals (Figure 2.4b).
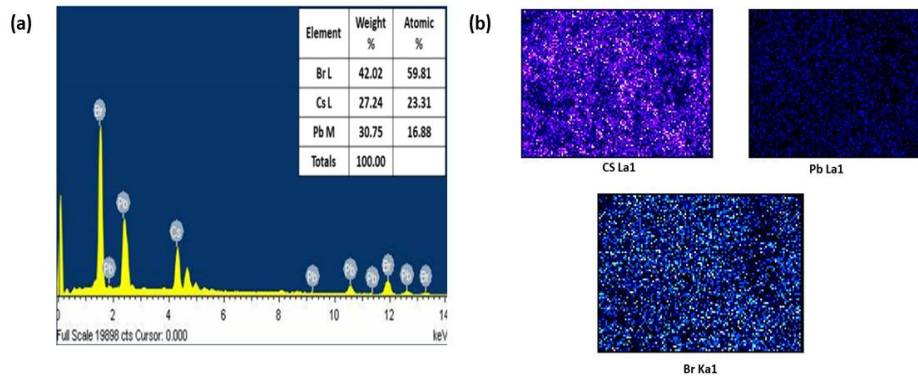
Figure 2.4 (a) EDX spectra of CsPbBr$_3$ with the inset image show the elemental ratios, and (b) Elemental mapping image of elements Cs, Pb, and Br

2.3.1.3 X-ray Photoelectron spectroscopy (XPS) analysis

The high-resolution X-ray photoelectron spectroscopy (XPS) were used for the detection of Cs, Pb, and Br elements in the perovskite CsPbBr$_3$ lattice. The binding energy that appeared at 738 eV and 724 eV are corresponding to Cs 3d$_{3/2}$ and Cs 3d$_{5/2}$, respectively (Figure 2.5a). The binding energies at 143.2 eV and 138.2 eV are attributed due to Pb 4f $_{5/2}$ and Pb 4f $_{7/2}$, respectively (Figure 2.5b). The Br 3d peak is submerged into two sub-peaks Br 3d$_{3/2}$ and Br 3d$_{5/2}$ corresponding to 68.94 and 67.52 eV, respectively (Figure 2.5c) [44].
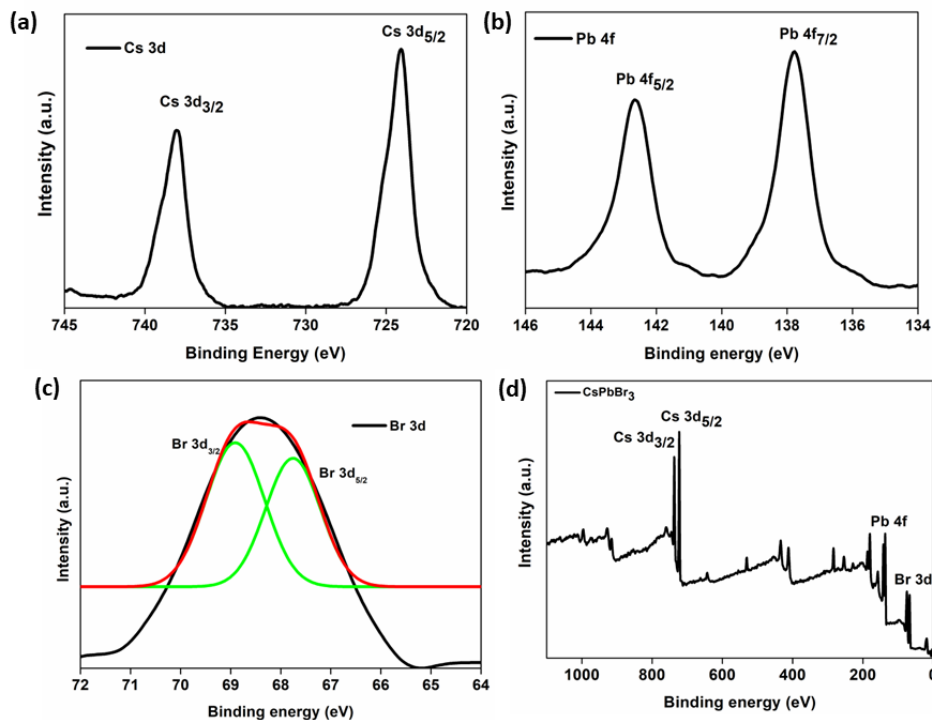

Figure 2.5 XPS survey of (a) Cs 3d spectrum, (b) Pb 4f spectrum, (c) Br 3d spectrum, and (d) prepared CsPbBr$_3$ spectrum

2.3.2 Morphological analysis

2.3.2.1 SEM analysis

The morphology of the perovskite crystals was elucidated by SEM analysis. As shown in Figure 2.6, the synthesized $CsPbBr_3$ crystals have an orthorhombic-shaped structure with an average crystal size of 1.6 μM.
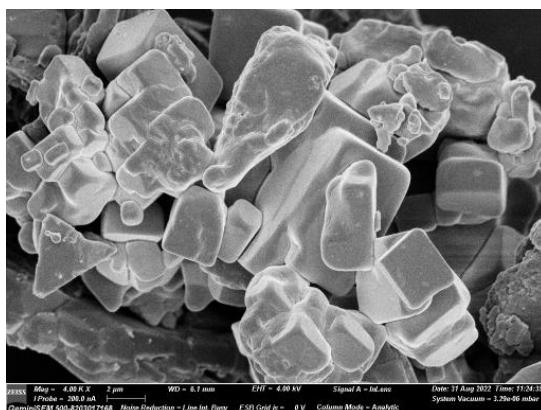

Figure 2.6 SEM image of $CsPbBr_3$

2.3.2.2 TEM analysis

The crystal structure, lattice spacing, and size of the perovskite crystals were further confirmed by Transmission Electron Microscopy (TEM) analysis. The TEM image of $CsPbBr_3$ represents an orthorhombic-shaped structure with an average particle size of 1.64 μm (Figure 2.7a). The selected area diffraction pattern (SAED) of the lattice structure with an interplanar spacing of 0.40 nm corresponds to the (110) plane of synthesized perovskite (Figure 2.7b). The TEM image indicates the high crystallinity of the microcrystals [45].
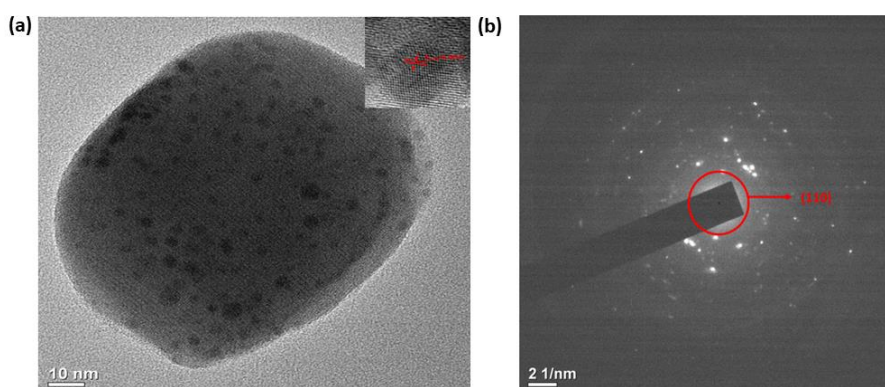

Figure 2.7 (a) TEM images of $CsPbBr_3$ with the interplanar distances of lattice fringes are shown in the inset image, and (b) the selected area diffraction (SAED) pattern of $CsPbBr_3$

2.3.3 Optical analysis

The optical properties of CsPbBr$_3$ were studied and it was observed that the perovskite exhibited a characteristic optical absorption peak at 440 nm (2.6 eV) and had a sharp emission peak at 520 nm with 20 nm full-width half maxima (FWHM). From the inset image (Figure 2.8), the perovskite dispersion emitted a bright, green-coloured irradiation of a 365 nm UV lamp (right) and pale orange colour daylight (left). The calculated fluorescence quantum yield (PLQY) of the CsPbBr$_3$ was 60%. In addition, the lifetime of CsPbBr$_3$ in an excited state was calculated [46]. As shown in Figure 2.9, the decay curves are well-fitted in a bi-exponential decay. The respective graphs constitute two components with the faster component τ_1 and the slower component τ_2. From the literature [45], it is found that the faster component τ_1 is due to the direct radiative excitation recombination from the conduction band to the valence band, and the slower component τ_2 is due to the non-radiative excitation recombination from the conduction band to the surface defects or from defects to defects, respectively. The high value of τ_1 revealed that the lifetime radiation was mainly due to direct excitation recombination and almost unrestricted by the non-radiative surface defects which might also be accountable for the higher value of quantum yield of MHPs. The calculated average lifetime of CsPbBr$_3$ was found as 8.76 ns (Table 2.1).
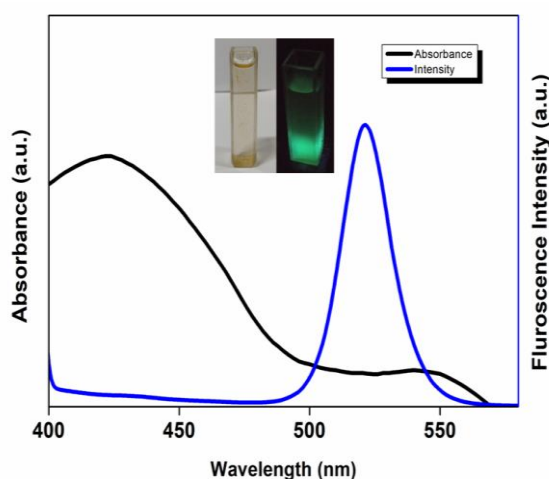

Figure 2.8 Luminescence and absorbance spectra of CsPbBr$_3$ dispersion with the inset images display the colour of dispersion under the irradiation of UV-lamp (right) and day-light (left)
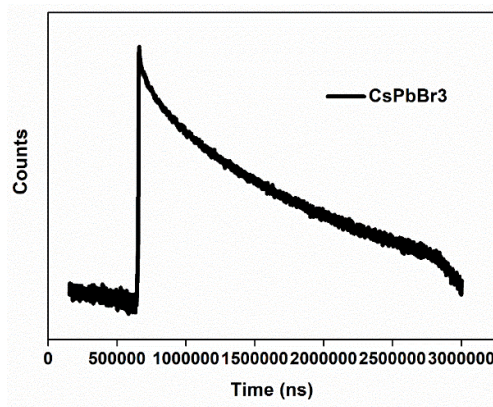
Figure 2.9 Time-resolved Photo-luminescence decay graph of CsPbBr$_3$

Table 2.1 Summary of luminescence results of passivated CsPbBr$_3$

Material	FWHM	PLQY (%)	λ_{max} (absorption)	λ_{max} (luminescence)	Band gap
CsPbBr$_3$	20 nm	60	530 nm	520 nm	2.6 eV

2.3.4 Study of stability of CsPbBr$_3$

The stability of the CsPbBr$_3$, the proposed sensor concerning time by recording the luminescence intensity in different time intervals within 25 min. Only 12.1% percentage degradation was found in the perovskite dispersion under 80% humid conditions (Figure 2.10a). Later the photostability test of the perovskite dispersion was investigated by illuminating a 365 nm UV-lamp for a limit of 8 hours. From PL intensity (Figure 2.10b), the calculated percentage degradation of CsPbBr$_3$ was found as 53.89%. The respective results demonstrate the stability of the designed sensor in a normal environment.
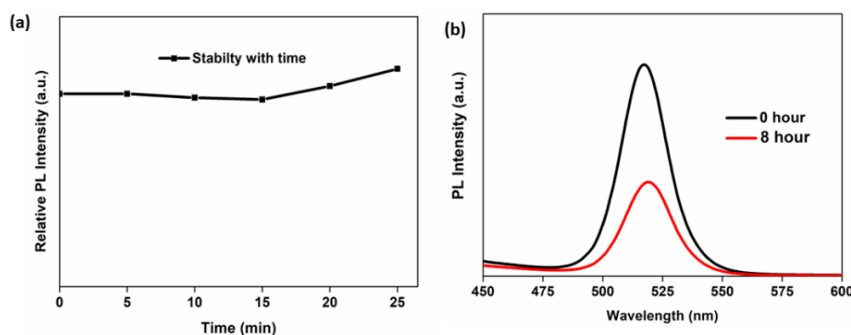

Figure 2.10 (a) Stability of CsPbBr$_3$ dispersion concerning time under 80% humid conditions and (b) Photostability of CsPbBr$_3$ dispersion under the illumination of 365 nm wavelength UV-lamp

2.3.5 Sensitivity of CsPbBr$_3$ towards UA

The easy preparatory method and excellent optical performance make CsPbBr$_3$ moiety a potential fluorescence probe toward target molecules. The sensing experiments were performed with the addition of a different amount of UA into a perovskite dispersion in toluene (0.1 mmol of CsPbBr$_3$ into 10 mL toluene). 3 mL of the above suspension was placed in a quartz cuvette and 50 µL of UA solution with known concentration is added to that solution. The fluorescence spectra were measured with an excitation wavelength of 380 nm. It was found that the fluorescence intensity of CsPbBr$_3$ gradually quenched with the addition of UA concentration ranging from 0.0031 to 1.33 µM (Figure 2.11a). Since there was no significant shift of the emission peak, the study implied that the possibility of intermolecular charge transfer was less during the sensing process [47]. The quenching efficiency was further calculated using the Stern-Volmer equation:

$$\frac{I_0}{I} = 1 + K_{sv}[C_{UA}]$$

In the above equation, I$_0$ is the initial PL intensity of CsPbBr$_3$ without adding the analyte UA, and I is the luminescence intensity of CsPbBr$_3$ with the addition of UA. C$_{UA}$ is the added concentration of UA and K$_{sv}$ is the Stern Volmer constant of the analyte. It was seen that the PL intensity and UA concentration were well fitted in the linear equation I$_0$/I = 1.36 + 4.14 [C_{UA}] with a correlation efficiency of 0.98 (Figure 2.11b). From the titration data, the limit of detection was calculated (3σ/K, where σ is the standard deviation for blank samples of repeat times n = 8 and K is the slope of the calibration curve) and found as 62.7 ppb. The calculated LOD of the system for UA detection is much lower compared to some other reported sensor probes (Table 2.2). The Stern-Volmer constant for titration data was found to be 4.14×10^6 M^{-1}.
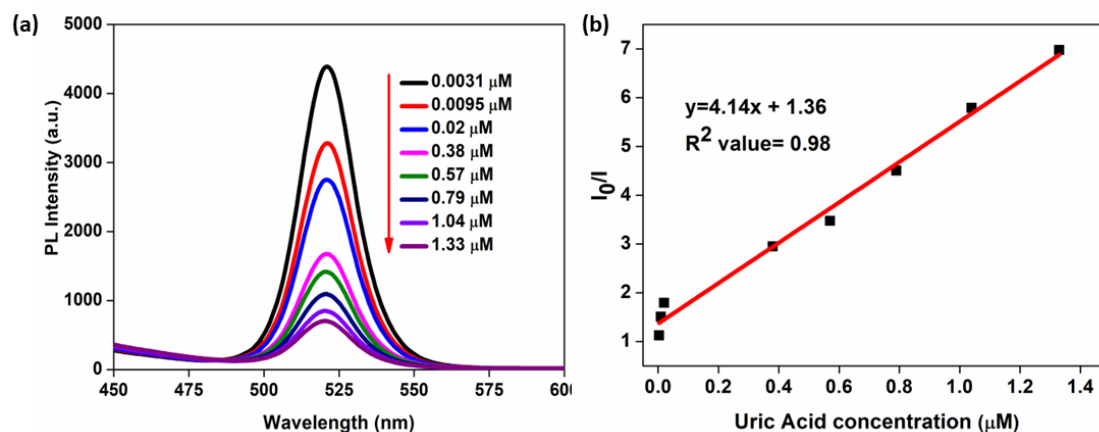
Figure 2.11 (a) Change in the PL spectra of CsPbBr$_3$ with the addition of UA, and (b) Stern-Volmer plots of the respective titration

Table 2.2 A Comparative study of a few fluorescence sensor probe systems for detection of UA

Entry	Sensor probe	LOD (μM)	Ref
1	CsPbBr$_3$	0.373	This work
2	Cu^{2+} @ MIL-91 (Al: Eu)	1.6	48
3	N-MWCNTs/ PtNPs	2.1	49
4	Xerogel	<10	50
5	AuNCs	6.6	51
6	Uricase/HRP-CdS QDs	125	52
7	NaYF$_4$:Yb^{3+}, Tm^{3+}	6.7	53
8	Carbon quantum dot/o-phenylenediamine	0.5	54
9	Heparin sulfur quantum dot	0.56	55
10	Silicon nanoparticles	0.75	56
11	Hydroxy functionalized boron nitride nanosheet	0.016	57
12	Fe, Co, N – co-doped Carbon dot	0.05	58
12	Yb3+, Er3+ and Tm3+ co-doped NaYF4	2.86	59
14	Carbon dot entrapped in Cr-MOF	1.3	60
15	Eu-MOF	0.689	61
16	UiO-PSM	0.0023	62
17	COOH-nanoflakes	1	63

18	CdTe capped with (glutathione,3-mercaptopropionic acid, and thio-glycerol)	0.1	64
19	Luminol-terbium	0.028	65
20	Carbon-dot with MnO_2	0.045	66
21	Carbon-dot with MONT	4.3	67
22	3-mercaptopropionic acid capped ZnS: Zn-CuS	0.044	68

In the fluorescence sensing process, the measurement of response time is an important parameter. The response time was evaluated after the addition of 0.57 μM of UA to the $CsPbBr_3$ dispersion. After adding the UA, the fluorescence intensity of $CsPbBr_3$ decreased rapidly and became stable after the 30 s (Figure 2.12). Hence, the response time for the target analyte UA was found 30 s. A minimum of 30 min incubation period is required in the clinical enzyme-based diagnosis of UA [69]. Therefore, it indicates that the $CsPbBr_3$ sensor probe have a faster response to UA and better potential sensor to be used in clinical diagnosis.
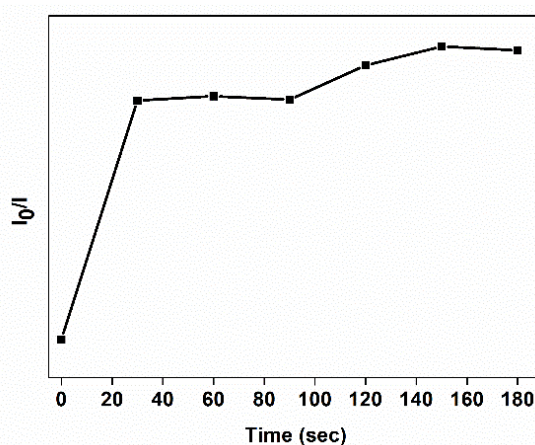

Figure 2.12 Response time measurement of $CsPbBr_3$ towards UA sensing

To study the effect of pH during UA titration, fluorescence intensities of $CsPbBr_3$ were measured at different pH conditions (pH = 2, 7, and 12). In case pH=2 (acidic condition), the sensor probe failed to perform any detection, and this can be understood as degradation of $CsPbBr_3$ in an acidic medium because of the leaching of Br^- ion (Figure 2.13a). However, the method demonstrated the positive activity in pH = 7 (neutral conditions). Thus, the optimum pH for the sensing study can be maintained at pH = 7. Similarly, the designed sensing

protocol was also functional to detect the analyte uric acid in a basic medium (pH = 12).

In addition, the sensing performance was also examined in 0.1 M different buffer solutions {(acidic: HCl + KCl, pH = 2), (neutral: phosphate, pH = 7), and (basic: $NaHCO_3$ and Na_2CO_3 pH = 10.6). Like the pH results, the sensing performance was failed in an acidic buffer because of leaching of Br- ion. Gratifyingly, our design was compatible with neutral and basic buffer conditions (Figure 2.13b).
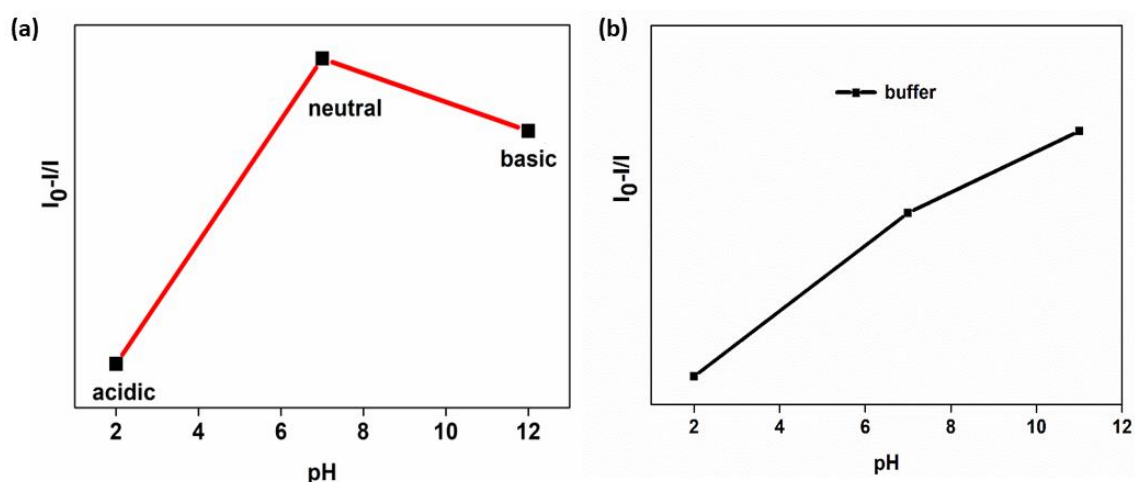

Figure 2.13 (a) Effect of pH on the PL quenching of CsPbBr$_3$ towards UA, and (b) Effect of different buffer solutions on the sensing performance of CsPbBr$_3$

2.3.6 Selective sensing of passivated CsPbBr$_3$

In sensor development, selectivity is always one of the challenging problems. To study the selectivity of CsPbBr$_3$ towards UA detection, various common biomolecules such as purines (adenine), amino acids (glycine, alanine, cystine, aspartic acid), glucose, hippuric acid, creatinine, and inorganic chloride salts (Na^+, K^+) were selected as the potential interfering counterparts. The fluorescence response was recorded in the presence of the interfering analytes with the same concentrations as UA was tested. The tested counterparts showed an extremely weak influence on CsPbBr$_3$ emission as compared to UA (Figure 2.14). These selective results suggested that CsPbBr$_3$ owes high selectivity and sensitivity towards UA molecules in biological samples without separating the UA from the tested interfering analyte and therefore, the sensing method is highly selective.
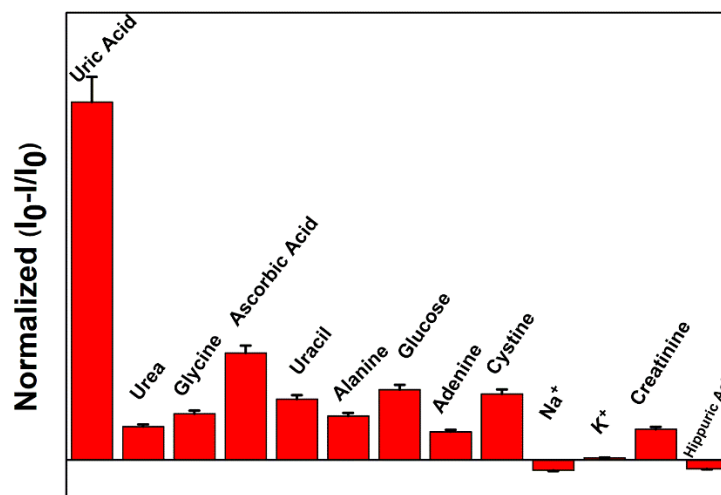
Figure 2.14 Selectivity profile of CsPbBr$_3$ towards UA and different biologically relevant interfering molecules and metal ions

2.3.7 Sensing mechanism of CsPbBr$_3$ towards UA

The reason behind the high selectivity and sensitivity of CsPbBr$_3$ towards UA was explored in the above-mentioned discussion. Since, upon addition of UA to the perovskite dispersion, there is no remarkable shifting of absorption and emission peak excludes the possibility of any charge transfer between the two interacting partners. Therefore, intermolecular charge transfer (ICT) will not be the cause of quenching. Also, it was observed that there was not any spectral overlap between the emission spectra of fluorophore CsPbBr$_3$ and the absorption spectra of the analyte UA in (Figure 2.15a). From these observations, the probability of the Förster resonance energy transfer (FRET) mechanism is very less in the sensing process [47].

Later, FT-IR spectra of different concentrations of UA-incorporated CsPbBr$_3$ were investigated. The characteristic absorption peaks at 1613 cm^{-1} and 1290 cm^{-1} appeared due to the stretching vibration of the C=O and C-N amide functional groups of uric acid (Figure 2.15b) depicts the adsorption of UA over CsPbBr$_3$ surface [69]. In (Figure 2.15a) it was seen that with increasing concentrations of UA to the CsPbBr$_3$ solution (0.1 mmol), the intensity of the respected UV peak gradually decreased. A similar response was also observed in the solid-state absorption spectra. From the XRD spectra (Figure 2.16b), it could be distinctly observed the disappearance of the peak corresponding to the (110) plan may be due to the possibility of structural degradation of CsPbBr$_3$. The structural degradation was also confirmed by FE-SEM images (Figure 2.17a-b). It is observed that the homogeneous orthorhombic-shaped

crystals of CsPbBr₃ changes to some non-uniform aggregation morphologies after the addition of UA.
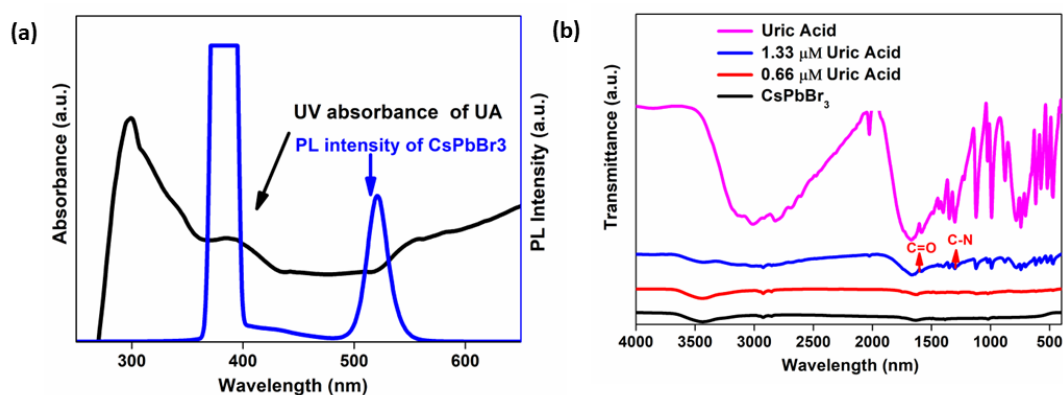

Figure 2.15 (a) Spectral overlap between the emission spectrum of (0.1 mmol) of CsPbBr₃ with the absorbance of (0.1 mmol) of UA and (b) FT-IR spectra of CsPbBr₃ titrated with various concentrations of UA
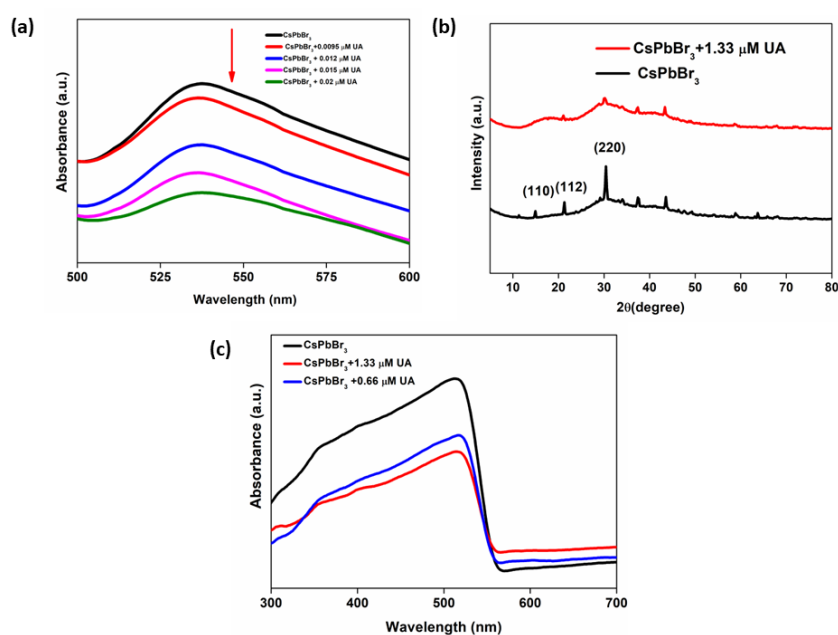

Figure 2.16 (a) The absorbance of CsPbBr₃ (0.1 mmol) in toluene in the presence of various concentrations of UA, (b) XRD spectra of CsPbBr₃ after exposure to 1.33 μM of UA, and (c) solid-state UV-Vis absorption of CsPbBr₃ titrated with various concentrations of UA
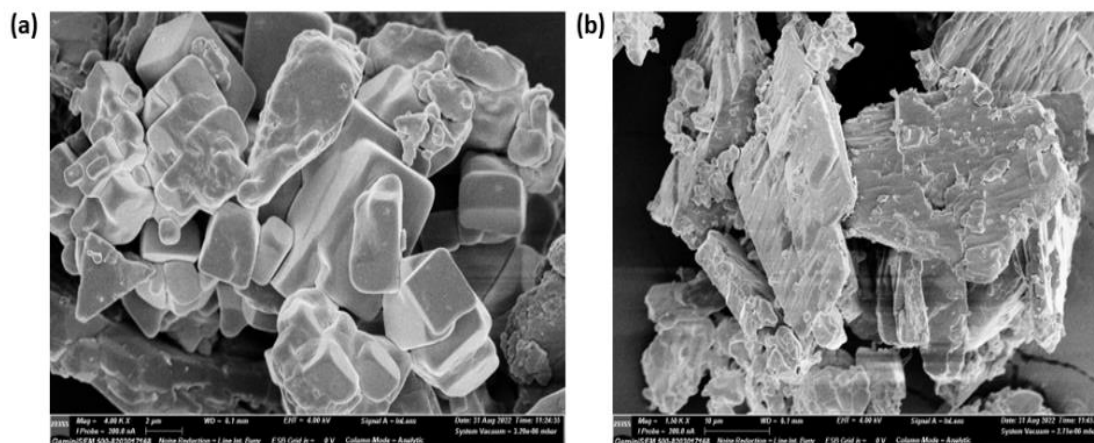
Figure 2.17 (a) FE-SEM image of CsPbBr₃, and (b) FE-SEM image of structural degradation after adding UA to CsPbBr₃

Moreover, the elemental mapping images of CsPbBr₃ after exposing UA was examined. The results displayed the images of elements C, N, and O uniformly distributed in the CsPbBr₃-UA crystal lattice (Figure 2.18).
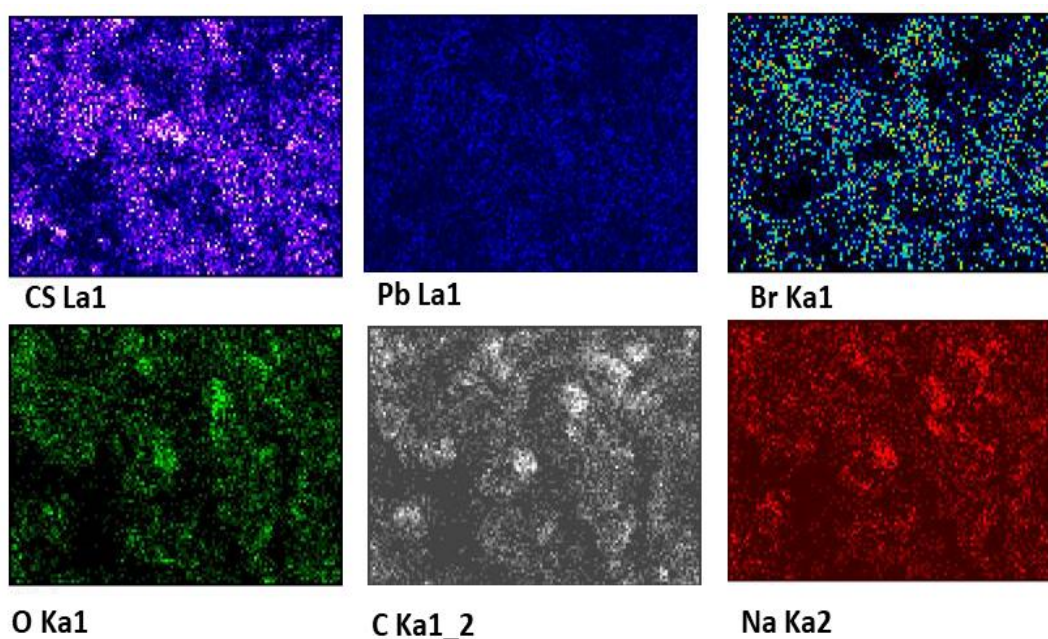

CS La1 Pb La1 Br Ka1

O Ka1 C Ka1_2 Na Ka2

Figure 2.18 Elemental mapping images of CsPbBr₃-UA

Further, the mechanism of the sensing process was further investigated through the time-resolved photoluminescence spectra (TRPL) under the excitation wavelength of 380 nm (Figure 2.19). In this study, it was noticed that the decay plots of the fluorescence were well-fitted in a bi-exponential decay. The calculated average lifetime of CsPbBr₃ was found 8.76 ns, but with the

addition of 0.66 μM and 1.33 μM UA; the value decreased to 8.64 ns and 8.15 ns (Table 2.3). Their respective line charts are also plotted (Figure 2.20). The less lifetime of the $CsPbBr_3$ in presence of UA indicates the sensor undergoes the dynamic quenching process. The H-bonding interaction most likely takes place between $CsPbBr_3$ and UA indicating some non-radiative decay pathways (Figure 2.21). The Br^- ion of $CsPbBr_3$ interacts with the H-atom of UA and leads to some anionic vacancies. And similarly, the interaction of Pb^{2+} with the N and O atoms of UA creates some cationic vacancies. These vacancies trigger the charge recombination and thereby, leading to the quenching of the emission peak at 520 nm [24,33,70].

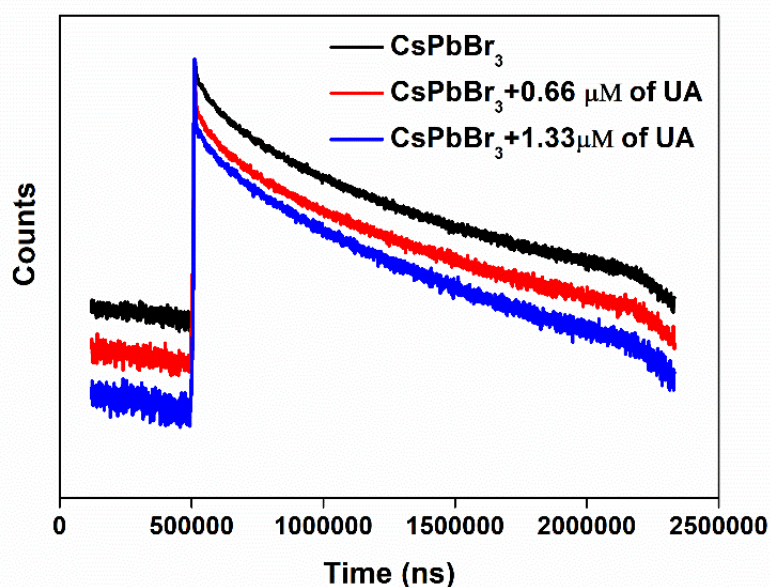**Figure 2.19** Time-resolved photoluminescence (TRPL) spectra of $CsPbBr_3$ (0.1 mmol) in the absence and presence of various concentrations of UA

Table 2.3 Concentration-dependent lifetime values

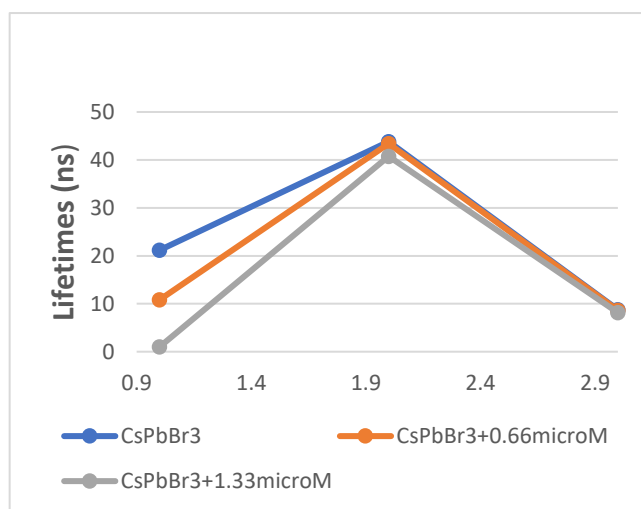| System	τ_1 (ns)	τ_2 (ns)	τ_{av} (ns)
$CsPbBr_3$	21.19	10.95	8.76
$CsPbBr_3$ + 0.66μM	10.8	21.7	8.64
$CsPbBr_3$ + 1.33μM	1.01	20.3	8.15

Figure 2.20 Line chart of the respective lifetimes of systems
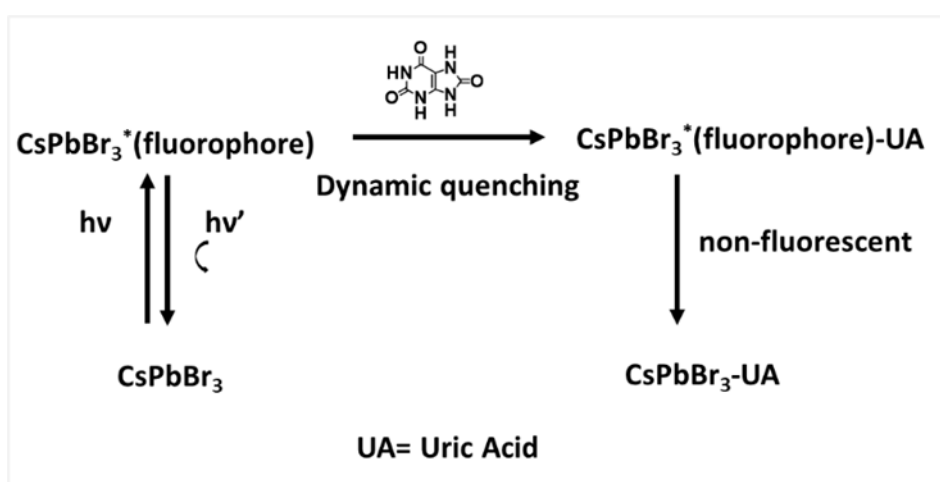
Figure 2.21 Dynamic quenching of the fluorophore of CsPbBr₃ via quencher UA

2.3.8 Colorimetric sensing studies

Furthermore, the study is extended its scope towards colorimetric method for the sensing process. During the analysis period, it was observed that gradual colour change occurred after adding different concentrations of UA ranging from concentration (0 µM to 0.57 µM) to the perovskite dispersion under the illumination of a 365 nm UV-lamp (Figure 2.22). The change in colour indicates some electronic changes after UA addition which may be due to interactions between surface ions of CsPbBr₃ and UA leading to some anion and cation vacancies. From the naked eye colour changing experience, it could be

concluded that the designed perovskite system can be also used as colorimetric method.
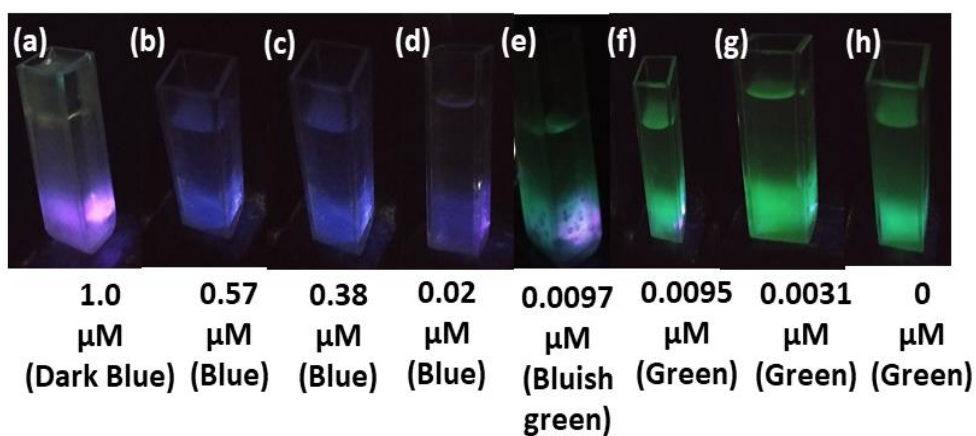

Figure 2.22 Photographs of perovskite solution under the UV emitting lamp of 365 nm wavelength after applying a volume of 3 mL (0.1 mmol CsPbBr$_3$) with different concentrations of UA

2.3.9 Sensing study of CsPbBr$_3$ on paper substrate

After the colorimetric method, a paper sensor technique was fabricated to detect UA by using a round paper with a diameter of 1cm×1cm. 1 mL of CsPbBr$_3$ dispersion (0.1 mmol in 10 mL toluene) was dispersed on a paper substrate and exposed to air for drying. Later, a solution of 1.33 μM UA was added to the CsPbBr$_3$-exposed paper. As shown in Figure 2.23, a specific color changes from green to blue was observed like the liquid phase observation. From this experiment, the present sensor also can be able to detect UA in paper substrate with naked eye without needing any sophisticated analytical instruments.
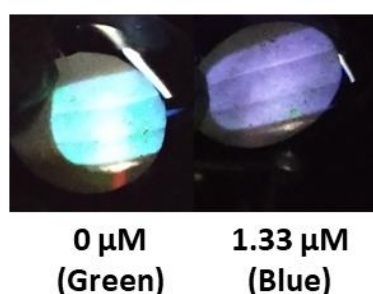

Figure 2.23 Photographs of test - paper under the UV emitting lamp of 365 nm wavelength after applying a fixed volume of 1 mL (0.1 mmol CsPbBr$_3$) with and without a concentration of 1.33 μM of UA

2.3.10 Control experiment in water

The applicability of the designed sensor was further validated in the aqueous environment. The sensing experiments were performed with the addition of UA dispersion in a water-toluene biphasic mixture. Firstly, UA (0.1 mmol) was dispersed in 10 mL water, and 1 mL of the solution was further mixed with 2 mL toluene in a volume ratio of (1:2). The respective luminescence intensity was measured with an excitation wavelength of 380 nm. In this study, it was noticed that the luminescence intensity of 3 mL CsPbBr$_3$ solution (0.1mmol in 10 mL toluene) was quenched gradually with the addition of target analyte UA dispersion (Figure 2.24a). In addition, a control experiment was performed to check the applicability of the method in the aqueous environment, where gradually added of H$_2$O and toluene in the same volume ratio to the perovskite suspension in toluene. Up to 250 µL the luminescence intensity of perovskite was increased in contrast to the change upon the addition of UA (Figure 2.24b).
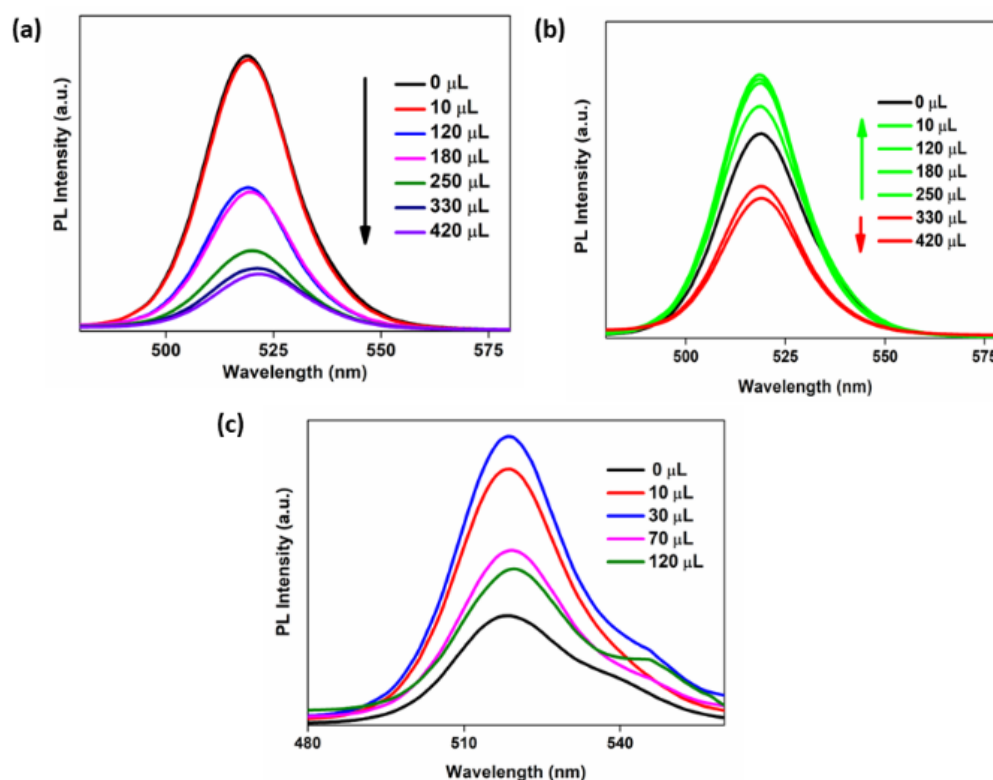

Figure 2.24 Validation of the designed sensor (a) upon the addition of different volumes of UA (dispersed in water) and toluene mixed in a volume ratio of 1:2 (b) upon the addition of different volumes of water and toluene mixture mixed (c) The PL intensity of CsPbBr$_3$ with the addition of different volumes of water

The difference in fluorescence behaviour proves the applicability of $CsPbBr_3$ dispersion toward UA detection in aqueous environments. The stability of the sensor was also investigated by measuring fluorescence intensity with the addition of different volumes of water to the perovskite dispersion. The addition of water also shows similar results where the intensity of the PL peak increased (Figure 2.24c). The results also indicate the aqueous stability of the proposed sensor probe. The increased PL intensity may be attributed due to the improved crystallization process of $CsPbBr_3$ in the bi-phasic medium [71].

2.4 Validation of the proposed sensor in real samples

The practical ability of the proposed sensor was further investigated in real sample assay. For this purpose, human blood serum samples (collected from the Health Centre of Tezpur University) were used to validate our proposed sensor in fluorescence assay. Prior to analysis, the samples were further diluted with 100-fold dilution. To the diluted serum, different known concentrations of UA were added. The details of the results are outlined (Table 2.4). The calculated favourable recoveries of 100%, 105.26%, and 97.36 % were obtained. This part of analysis suggested about the good reliability of the proposed sensor for detecting UA in real samples for clinical diagnosis.

Table 2.4 Determination of UA in human blood serum using $CsPbBr_3$

Dilution	Added UA (µM)	Found UA (µM)	Recovery %	RSD %
	0.0095	0.01	105.26	0.54
100-fold	0.02	0.02	100	1.1
	0.38	0.37	97.26	5.2

2.5 Conclusion

In summary, this chapter discussed the synthesis of the inorganic halide perovskite $CsPbBr_3$ and its application as fluorescence sensor to detect uric acid. The developed sensing method exhibited high selectivity and sensitivity. The quenching mechanism of $CsPbBr_3$ for UA was explained by the dynamic quenching mechanism. The designed sensor was significantly able to detect UA

in the range 0.0031-1.33 µM with an ultralow detection limit of 62.7 ppb and a fast response time of the 30s. Thia perovskite showed a specific colour change with exposure to the increasing concentrations of UA which is demonstrated as a colorimetric sensor probe for the detection of UA. A paper sensor was also fabricated to detect UA. The practical applicability of the sensor probe was further studied by the detection of UA in human blood serum. From the favourable recoveries, this chapter shows an alternative probe that can be applied in biomedical fields to detect UA-related diseases in clinical diagnosis.

2.6 Bibliography

[1] Zhang, H., Dai, P., Huang, L., Huang, Y., Huang, Q., Zhang, W., Wei, C., and Hu, S. A nitrogen-doped carbon dot/ferrocene@β-cyclodextrin composite as an enhanced material for sensitive and selective determination of uric acid. *Analytical Methods*, 6(8):2687-2691, 2014.

[2] Bergamini, C., Cicoira, M., Rossi, A., and Vassanelli, C. Oxidative stress and hyperuricaemia: pathophysiology, clinical relevance, and therapeutic implications in chronic heart failure. *European Journal Of Heart Failure*, 11(5):444-452, 2009.

[3] Chauhan, N. and Pundir, C. S. An amperometric uric acid biosensor based on multiwalled carbon nanotube–gold nanoparticle composite. *Analytical Biochemistry*, 413(2):97-103, 2011.

[4] Zhang, F., Ma, P., Deng, X., Sun, Y., Wang, X., and Song, D. Enzymatic determination of uric acid using water-soluble CuInS/ZnS quantum dots as a fluorescent probe. *Microchimica Acta*, 185:1-8, 2018.

[5] Westley, C., Xu, Y., Carnell, A. J., Turner, N. J., and Goodacre, R. Label-free surface enhanced Raman scattering approach for high-throughput screening of biocatalysts. *Analytical Chemistry*, 88(11):5898-5903, 2016.

[6] Lu, Q., Deng, J., Hou, Y., Wang, H., Li, H., and Zhang, Y. One-step electrochemical synthesis of ultrathin graphitic carbon nitride nanosheets and their application to the detection of uric acid. *Chemical Communications*, 51(61):12251-12253, 2015.

[7] Liu, Y., Li, H., Guo, B., Wei, L., Chen, B., and Zhang, Y. Gold nanoclusters as switch-off fluorescent probe for detection of uric acid based on the inner filter effect of hydrogen peroxide-mediated enlargement of gold nanoparticles. *Biosensors and Bioelectronics*, 91:734-740, 2017.

[8] Andreadou, E., Nikolaou, C., Gournaras, F., Rentzos, M., Boufidou, F., Tsoutsou, A., Zournas, C., Zissimopoulos, V., and Vassilopoulos, D. Serum uric acid levels in patients with Parkinson's disease: their relationship to treatment and disease duration. *Clinical Neurology and Neurosurgery*, 111(9):724-728, 2009.

[9] Ghosh, T., Sarkar, P., and Turner, A. P. A novel third generation uric acid biosensor using uricase electro-activated with ferrocene on a Nafion coated glassy carbon electrode. *Bioelectrochemistry*, 102:1-9, 2015.

[10] Westley, C., Xu, Y., Thilaganathan, B., Carnell, A. J., Turner, N. J., and Goodacre, R. Absolute quantification of uric acid in human urine using surface enhanced Raman scattering with the standard addition method. *Analytical Chemistry*, 89(4):2472-2477, 2017.

[11] Kim, M.-C., Kwak, J., and Lee, S. Y. Sensing of uric acid *via* cascade catalysis of uricase and a biomimetic catalyst. *Sensors and Actuators B: Chemical*, 232:744-749, 2016.

[12] Zhou, S., Zuo, R., Zhu, Z., Wu, D., Vasa, K., Deng, Y., and Zuo, Y. An eco-friendly hydrophilic interaction HPLC method for the determination of renal function biomarkers, creatinine, and uric acid, in human fluids. *Analytical Methods*, 5(5):1307-1311, 2013.

[13] Kubalczyk, P. and Bald, E. Method for determination of total cysteamine in human plasma by high performance capillary electrophoresis with acetonitrile stacking. *Electrophoresis*, 29(17):3636-3640, 2008.

[14] Kuśmierek, K. and Bald, E. Measurement of reduced and total mercaptamine in urine using liquid chromatography with ultraviolet detection. *Biomedical Chromatography*, 22(4):441-445, 2008.

[15] Chen, J.-C., Chung, H. H., Hsu, C. T., Tsai, D. M., Kumar, A., and Zen, J. M. A disposable single-use electrochemical sensor for the detection of uric acid in human whole blood. *Sensors and Actuators B: Chemical*, 110(2):364-369, 2005.

[16] Mazzara, F., Patella, B., Aiello, G., O'Riordan, A., Torino, C., Vilasi, A., and Inguanta, R. Electrochemical detection of uric acid and ascorbic acid using r-GO/NPs based sensors. *Electrochimica Acta*, 388:138652, 2021.

[17] Liu, C. S., Li, J., and Pang, H. Metal-organic framework-based materials as an emerging platform for advanced electrochemical sensing. *Coordination Chemistry Reviews*, 410:213222, 2020.

[18] Cao, S., Zheng, S., and Pang, H. Ultrathin nanosheet-assembled accordion-like Ni-MOF for hydrazine hydrate amperometric sensing. *Microchimica Acta*, 187:1-9, 2020.

[19] Hwang, S. M., Kim, M. S., Lee, M., Lim, M. H., and Kim, C. Single fluorescent chemosensor for multiple targets: sequential detection of Al^{3+} and pyrophosphate and selective detection of F^- in near-perfect aqueous solution. *New Journal of Chemistry*, 41(24):15590-15600, 2017.

[20] Yin, D., Li, X., Ma, Y., and Liu, Z. Targeted cancer imaging and photothermal therapy *via* monosaccharide-imprinted gold nanorods. *Chemical Communications*, 53(50):6716-6719, 2017.

[21] Liu, R., Zhang, L., Chen, Y., Huang, Z., Huang, Y., and Zhao, S. Design of a new near-infrared ratio-metric fluorescent nanoprobe for real-time imaging of superoxide anions and hydroxyl radicals in live cells and in situ tracing of the inflammation process *in vivo*. *Analytical Chemistry*, 90(7):4452-4460, 2018.

[22] Zhang, K., Song, S., Yang, L., Min, Q., Wu, X., and Zhu, J. J. Enhancing intracellular microRNA imaging: a new strategy combining double-channel exciting single colour fluorescence with the target cycling amplification reaction. *Chemical Communications*, 54(93):13131-13134, 2018.

[23] Dalapati, R. and Biswas, S. A pyrene-functionalized metal–organic framework for nonenzymatic and ratio-metric detection of uric acid in biological fluid *via* conformational change. *Inorganic Chemistry*, 58(9):5654-5663, 2019.

[24] Dey, N. and Bhattacharya, S. Nanomolar level detection of uric acid in blood serum and pest-infested grain samples by an amphiphilic probe. *Analytical Chemistry*, 89(19):10376-10383, 2017.

[25] Zhang, T., Sun, X., and Liu, B. Synthesis of positively charged CdTe quantum dots and detection for uric acid. *Spectrochimica Acta Part A: Molecular and Biomolecular Spectroscopy*, 79(5):1566-1572, 2011.

[26] Zhao, C., Jiao, Y., Hu, F., and Yang, Y. Green synthesis of carbon dots from pork and application as nano-sensors for uric acid detection. *Spectrochimica Acta Part A: Molecular and Biomolecular Spectroscopy*, 190:360-367, 2018.

[27] Xiao, Z., Kerner, R. A., Zhao, L., Tran, N. L., Lee, K. M., Koh, T. W., Scholes, G. D., and Rand, B. P. Efficient perovskite light-emitting diodes featuring nanometre-sized crystallites. *Nature Photonics*, 11(2):108-115, 2017.

[28] Liang, J., Chen, D., Yao, X., Zhang, K., Qu, F., Qin, L., Huang, Y., and Li, J. Recent progress and development in inorganic halide perovskite quantum dots for photoelectrochemical applications. *Small*, 16(15):1903398, 2020.

[29] Cho, H., Jeong, S. H., Park, M. H., Kim, Y. H., Wolf, C., Lee, C. L., Heo, J. H., Sadhanala, A., Myoung, N., and Yoo, S. Overcoming the electroluminescence efficiency limitations of perovskite light-emitting diodes. *Science*, 350(6265):1222-1225, 2015.

[30] Yin, B. *Defect Chemistry and Ion Intercalation During the Growth and Solid-State Transformation of Metal Halide Nanocrystals*. Washington University, St. Louis, 2019.

[31] Song, J., Cui, Q., Li, J., Xu, J., Wang, Y., Xu, L., Xue, J., Dong, Y., Tian, T., and Sun, H. Ultralarge all-inorganic perovskite bulk single crystal for high-performance visible–infrared dual-modal photodetectors. *Advanced Optical Materials*, 5(12):1700157, 2017.

[32] Duan, J., Wang, M., Wang, Y., Zhang, J., Guo, Q., Zhang, Q., Duan, Y., and Tang, Q. Effect of side-group-regulated dipolar passivating molecules on $CsPbBr_3$ perovskite solar cells. *ACS Energy Letters*, 6(6):2336-2342, 2021.

[33] Kim, S. H., Kirakosyan, A., Choi, J., and Kim, J. H. Spectroscopic study on the interaction of organic-inorganic hybrid perovskite nanoparticles with linear aliphatic alcohols. *Dyes and Pigments*, 143:71-75, 2017.

[34] Chen, C., Cai, Q., Luo, F., Dong, N., Guo, L., Qiu, B., and Lin, Z. Sensitive fluorescent sensor for hydrogen sulfide in rat brain microdialysis *via* $CsPbBr_3$ quantum dots. *Analytical Chemistry*, 91(24):15915-15921, 2019.

[35] Xu, X., Wang, X., Liu, W., Wang, S., Jiang, H., Ma, S., Yuan, F., and Ma, N. Ambient Stable $CsPbBr_3$/ZnO Nanostructures for Ethanolamine Sensing. *ACS Applied Nano Materials*, 5(10):15030-15041, 2022.

[36] Huang, Y., Wang, S., Zhu, Y., Li, F., Jin, J., Dong, J., Lin, F., Wang, Y., and Chen, X. Dual-mode of fluorescence turn-on and wavelength-shift for methylamine gas sensing based on space-confined growth of methylammonium lead tribromide perovskite nanocrystals. *Analytical Chemistry*, 92(8):5661-5665, 2020.

[37] Chen, X., Hu, H., Xia, Z., Gao, W., Gou, W., Qu, Y., and Ma, Y. $CsPbBr_3$ perovskite nanocrystals as highly selective and sensitive spectrochemical probes for gaseous HCl detection. *Journal of Materials Chemistry C*, 5(2):309-313, 2017.

[38] Huangfu, C. and Feng, L. High-performance fluorescent sensor based on $CsPbBr_3$ quantum dots for rapid analysis of total polar materials in edible oils. *Sensors and Actuators B: Chemical*, 344:130193, 2021.

[39] Kong, Z. C., Liao, J. F., Dong, Y. J., Xu, Y. F., Chen, H. Y., Kuang, D. B., and Su, C. Y. Core@ shell $CsPbBr_3$@zeolitic imidazolate framework nanocomposite for efficient photocatalytic CO_2 reduction. *ACS Energy Letters*, 3(11):2656-2662, 2018.

[40] Brouwer, A. M. Standards for photoluminescence quantum yield measurements in solution (IUPAC Technical Report). *Pure and Applied Chemistry*, 83(12):2213-2228, 2011.

[41] Wang, S., Bi, C., Portniagin, A., Yuan, J., Ning, J., Xiao, X., Zhang, X., Li, Y. Y., Kershaw, S. V., and Tian, J. $CsPbI_3$/PbSe hetero-structured nanocrystals for high-efficiency solar cells. *ACS Energy Letters*, 5(7):240-2410, 2020.

[42] Ghaithan, H. M., Alahmed, Z. A., Qaid, S. M., Hezam, M., and Aldwayyan, A. S. Density functional study of cubic, tetragonal, and orthorhombic $CsPbBr_3$ perovskite. *ACS Omega*, 5(13):7468-7480, 2020.

[43] Zhang, M., Zheng, Z., Fu, Q., Chen, Z., He, J., Zhang, S., Yan, L., Hu, Y., and Luo, W. Growth, and characterization of all-inorganic lead halide perovskite semiconductor $CsPbBr_3$ single crystals. *CrystEngComm*, 19(45):6797-6803, 2017.

[44] Yuan, B., Li, N., Liu, J., Xu, F., Li, C., Juan, F., Yu, H., Li, C., and Cao, B. Improving the performances of $CsPbBr_3$ solar cells fabricated in ambient condition. Journal of Materials Science: Materials in Electronics, 31:21154-21167, 2020.

[45] Shu, Y., Wang, Y., Guan, J., Ji, Z., Xu, Q., and Hu, X. Amphiphilic Polymer Ligand-Assisted Synthesis of Highly Luminescent and Stable Perovskite Nanocrystals for Sweat Fluorescent Sensing. *Analytical Chemistry*, 94(13):5415-5424, 2022.

[46] Guan, Z., Chen, F., Liu, Z., L, P., Chen, M., Guo, M., Li, X., Teng, F., Chen, S., and Tang, A. Compositional engineering of multinary Cu–In–Zn-based semiconductor nanocrystals for efficient and solution-processed red-emitting quantum-dot light-emitting diodes. *Organic Electronics*, 74: 4651, 2019.

[47] Wang, T., Wei, X., Zong, Y., Zhang, S., and Guan, W. An efficient and stable fluorescent sensor based on APTES-functionalized $CsPbBr_3$ perovskite quantum dots for ultrasensitive tetracycline detection in ethanol. *Journal of Materials Chemistry C*, 8(35):12196-12203, 2020.

[48] Lian, X. and Yan, B. Phosphonate MOFs composite as off–on fluorescent sensor for detecting purine metabolite uric acid and diagnosing hyperuricuria. *Inorganic Chemistry*, 56(12):6802-6808, 2017.

[49] Tsierkezos, N. G., Othman, S. H., Ritter, U., Hafermann, L., Knauer, A., Köhler, J. M., Downing, C., and McCarthy, E. K. Electrochemical analysis of ascorbic acid, dopamine, and uric acid on noble metal modified nitrogen-doped carbon nanotubes. *Sensors and Actuators B: Chemical*, 231:218-229, 2016.

[50] Conway, G. E., Lambertson, R. H., Schwarzmann, M. A., Pannell, M. J., Kerins, H. W., Rubenstein, K. J., Dattelbaum, J. D., and Leopold, M. C. Layer-by-layer design and optimization of xerogel-based amperometric

first generation biosensors for uric acid. *Journal of Electroanalytical Chemistry*, 775:135-145, 2016.

[51] Wang, J., Chang, Y., Wu, W. B., Zhang, P., Lie, S. Q., and Huang, C. Z. Label-free and selective sensing of uric acid with gold nanoclusters as optical probe. *Talanta*, 152:314-320, 2016.

[52] Azmi, N. E., Ramli, N. I., Abdullah, J., Hamid, M. A. A., Sidek, H., Abd Rahman, S., Ariffin, N., and Yusof, N. A. A simple and sensitive fluorescence-based biosensor for the determination of uric acid using H_2O_2-sensitive quantum dots/dual enzymes. *Biosensors and Bioelectronics*, 67:129-133, 2015.

[53] Long, Q., Fang, A., Wen, Y., Li, H., Zhang, Y., and Yao, S. Rapid and highly sensitive uric acid sensing based on enzymatic catalysis-induced up conversion inner filter effect. *Biosensors and Bioelectronics*, 86:109-114, 2016.

[54] Yuan, C., Qin, X., Xu, Y., Shi, R., Cheng, S., and Wang, Y. Dual-signal uric acid sensing based on carbon quantum dots and o-Phenylenediamine. *Spectrochimica Acta Part A: Molecular and Biomolecular Spectroscopy*, 254:119678, 2021.

[55] Rong, S., Chen, Q., Xu, G., Wei, F., Yang, J., Ren, D., Cheng, X., Xia, X., Li, J., and Gao, M. Novel, and facile synthesis of heparin sulfur quantum dots *via* oxygen acceleration for ratio-metric sensing of uric acid in human serum. *Sensors and Actuators B: Chemical*, 353:131146, 2022.

[56] Wu, C., Zhu, L., Lu, Q., Li, H., Zhang, Y., and Yao, S. A dual-signal colorimetric and ratiometric fluorescent nanoprobe for enzymatic determination of uric acid by using silicon nanoparticles. *Microchimica Acta*, 186:1-8, 2019.

[57] Revabhai, P. M., Park, T. J., and Kailasa, S. K. One-step hydrothermal approach for synthesis of hydroxy functionalized boron nitride nanosheets for fluorescence detection of uric acid in biological samples. *Inorganic Chemistry Communications*, 148:110346, 2023.

[58] Li, F., Chen, J., Wen, J., Peng, Y., Tang, X., and Qiu, P. Ratio-metric fluorescence and colorimetric detection for uric acid using bifunctional carbon dots. *Sensors and Actuators B: Chemical*, 369:132381, 2022.

[59] Fang, A., Wu, Q., Lu, Q., Chen, H., Li, H., Liu, M., Zhang, Y., and Yao, S. Upconversion ratio-metric fluorescence and colorimetric dual-readout assay for uric acid. *Biosensors and Bioelectronics*, 86:664-670, 2016.

[60] Shatery, O. B. A. and Omer, K. M. Selectivity Enhancement for Uric Acid Detection *via* In Situ Preparation of Blue Emissive Carbon Dots Entrapped in Chromium Metal–Organic Frameworks. *ACS Omega*, 7(19):16576-16583, 2022.

[61] Han, L. J., Kong, Y. J., Hou, G. Z., Chen, H. C., Zhang, X. M., and Zheng, H. G. A europium-based MOF fluorescent probe for efficiently detecting malachite green and uric acid. *Inorganic Chemistry*, 59(10):7181-7187, 2020.

[62] Qu, S., Li and Z., Jia, Q. Detection of purine metabolite uric acid with picolinic-acid-functionalized metal–organic frameworks. *ACS Applied Materials & Interfaces*, 11(37):34196-34202, 2019.

[63] Mao, Z. Y., Zhu, L. N., Gao, J., Liu, J. J., Wei, Y. H., Li, X. Y., Yin, B. C., and Wang, J. A CoOOH nanoflake-based light scattering probe for the simple and selective detection of uric acid in human serum. *Analytical Methods*, 10(40):4951-4957, 2018.

[64] Jin, D., Seo, M. H., Huy, B. T., Pham, Q. T., Conte, M. L., Thangadurai, D., and Lee, Y. I. Quantitative determination of uric acid using CdTe nanoparticles as fluorescence probes. *Biosensors and Bioelectronics*, 77:359-365, 2016.

[65] Qi, W., Zhao, M., Fu, Y., He, H., Tian, X., Wu, D., Zhang, Y., and Hu, P. P. Fluorescent detection of uric acid through photoinduced electron transfer using luminol-terbium(III) nanoparticles synthesized *via* aggregation-induced fluorescence strategy. *Dyes and Pigments*, 172:107797, 2020.

[66] Yang, J., Huang, Z., Hu, Y., Ge, J., Li, J., and Li, Z. A facile fluorescence assay for rapid and sensitive detection of uric acid based on carbon dots and MnO_2 nanosheets. *New Journal of Chemistry*, 42(18):15121-15126, 2018.

[67] Xin, X., Zhang, M., Zhao, J., Han, C., Liu, X., Xiao, Z., Zhang, L., Xu, B., Guo, W., and Wang, R. Fluorescence turn-on detection of uric acid by a water-

stable metal–organic nanotube with high selectivity and sensitivity. *Journal of Materials Chemistry C*, 5(3):601-606, 2017.

[68] Wang, M., Niu, W., Wu, X., Li, L., Yang, J., Shuang, S., and Dong, C. Fluorescence enhancement detection of uric acid based on water-soluble 3-mercaptopropionic acid-capped core/shell ZnS: Cu/ZnS. *RSC Advances*, 4(48):25183-25188, 2014.

[69] Mujahid, A., Khan, A. I., Afzal, A., Hussain, T., Raza, M. H., Shah, A. T., and Zaman, W. Molecularly imprinted titania nanoparticles for selective recognition and assay of uric acid. *Applied Nanoscience*, 5:527-534, 2015.

[70] Huang, S., Guo, M., Tan, J., Geng, Y., Wu, J., Tang, Y., Su, C., Lin, C. C., and Liang, Y. Novel fluorescence sensor based on all-inorganic perovskite quantum dots coated with molecularly imprinted polymers for highly selective and sensitive detection of omethoate. *ACS Applied Materials & Interfaces*, 10(45):39056-39063, 2018.

[71] Li, P., Xie, W., Mao, W., Tian, Y., Huang, F., Xu, S., and Zhang, J. Luminescence enhancement of $CsPbBr_3$ quantum dot glasses induced by two unexpected methods: mechanical and hydration crystallization. *Journal of Materials Chemistry C*, 8(2):473-480, 2020.